Research Article

Nano Biomed Eng

Impact of Ionic Liquids on the Crystal Growth and Surface Morphology of Ruthenium-doped TiO_2 Nano Heterojunction Structures for Improved Photocatalytic Degradation of Evans Blue Dye and the Associated Antibacterial Activities

T. N. Ravishankar[1], A. Ananda[2], J. R. Adarsha[3], B. M. Shilpa[4]

[1] Department of Chemistry, B.M.S. College of Engineering, Bangalore, Karnataka 560019, India
[2] Department of Chemistry, Dayananda Sagar Academy of Technology & Management Udayapura, Bengaluru 560082, India
[3] Department of chemistry, Global Academy of Technology, Ideal Homes Township, Bangalore, Karnataka 560098, India
[4] Department of Psychology, Christ-Deemed to be University, Bangalore Kengeri Campus, Bangalore, Karnataka 560074, India

Corresponding author. E-mail: ravishankartn.chem@bmsce.ac.in

Received: Mar. 22, 2024; **Revised:** Apr. 30, 2024; **Accepted:** May 21, 2024

Citation: T.N. Ravishankar, A. Ananda, J.R. Adarsha, et al. Impact of ionic liquids on the crystal growth and surface morphology of ruthenium-doped TiO_2 nano heterojunction structures for improved photocatalytic degradation of Evans blue dye and the associated antibacterial activities. *Nano Biomedicine and Engineering*, 2025, 17(4): 570−588.

http://doi.org/10.26599/NBE.2024.9290093

Abstract

Novel Ru-doped TiO_2 nanocomposites (Ru/TiO_2 NCs) were synthesized at a 130 °C temperature and 24-h incubation period using hydrothermal methods with and without ionic liquids (ILs). NCs were synthesized using 1-butyl-2,3-dimethylimidazolium tetrafluoroborate as the ILs and titanium(IV) isopropoxide and ruthenium(III) nitrate as the precursors. The presence of Ru in the NCs was analyzed using different characterization techniques. Powder X-ray diffraction and transmission electron microscopy confirmed the presence of anatase and rutile phases as well as the nanocrystalline texture of the prepared Ru/TiO_2 NCs. The presence of Ru, Ti, and O was confirmed via energy-dispersive X-ray spectroscopy and X-ray photoelectron spectroscopy. The optical properties and bandgap energies of Ru/TiO_2 NCs were determined via ultraviolet (UV)–visible (Vis) diffuse reflectance spectroscopy; the optical properties exhibited a redshift in the optical response toward the visible region owing to the reduced bandgap energy of Ru/TiO_2 NCs in the visible region after doping Ru into the TiO_2 nanocrystalline structure. Scanning electron microscopy images revealed a highly voluminous and porous network of Ru/TiO_2 NCs. Moreover, different concentrations of Ru were doped into the TiO_2 matrix to investigate the photocatalytic and antibacterial activities. Among all the synthesized NCs, 0.3-wt% Ru/TiO_2 NCs exhibited high photocatalytic degradation efficiency and was therefore considered the optimum concentration. Moreover, it exhibited the highest BET surface area and quantum efficiency compared with other Ru/TiO_2 NCs. Results revealed that Ru/TiO_2 NCs synthesized via IL-assisted hydrothermal method, i.e., R_3TL, exhibited considerably enhanced photocatalytic and antibacterial activities compared to the NCs synthesized without the ILs, i.e., R_3TH. The inhibition pattern showed an excellent zone of inhibition ($p < 0.001$) in several strains with both NCs (R_3TL and R_3TH). However, Gram-positive *Staphylococcusaureus* exhibited a remarkably increased zone of inhibition (35 mm) compared with all the other strains used for R_3TH. In contrast, *Bacillus sp.* exhibited the second largest zone of inhibition (21 mm) for R_3TL after *S. aureus* (34 mm). In summary, this study emphasized the role of ILs and reaction mechanisms.

Keywords: Ru/TiO_2 nanocomposite; ionic liquid; hydrothermal method; photocatalytic degradation; antibacterial activity.

Introduction

Rapid industrialization has caused a considerable increase in water pollution globally [1]. Textile industry forms the backbone of India's economy; however, large amounts of organic dyes are released into water during textile dyeing. Most of these dyes are extremely noxious and non biodegradable, which impact animal and public health in addition to the biotic components of the aquatic ecosystem. Therefore, the quality of wastewater should be checked before its reuse [1]. Azo dyes containing one or more azo groups (–N=N–) with substituted aromatic rings are currently used for textile dyeing; however, these dyes are carcinogenic and non biodegradable in aerobic media [2]. These organic dyes can be removed from wastewater via coagulation, biodegradation, flocculation, chemical oxidation, and adsorption. In the past three decades [3], various adsorbents, such as activated carbon [4], clays [5, 6], and carbon nanotubes [7, 8], were used for dye adsorption; however, the associated cost is high, less stable and production of some toxic byproducts are involved [9]. Therefore, advanced oxidation processes were adopted, wherein transition metal–semiconductor nanophotocatalysts were used, as they produced OH radicals in-situ; these radicals oxidize the dyes present in wastewater into CO_2 and H_2O [10, 11]. Moreover, these photocatalysts are economical and nontoxic and their optical and electronic properties can be tuned by doping with nobel metals and controlling their particle size for multielectron transfer. They also exhibit high photocatalytic efficiency without considerable loss in photocatalytic activity and can therefore be recycled [12]. These photocatalysts produce chemical energy after light irradiation [13, 14], therefore initiating a photochemical reaction. As a result, they can be used for sustainable reactions such as water remediation, electrolysis, and environmental remediation. Many traditional transition-metal oxides such as CaO, MgO, SnO_2, ZnO, and TiO_2 have also been effectively used in such applications [15, 16]. TiO_2 NPs are abundant and economical and have high chemical, photo stability and the redox potential of water aligns with the positions of valence and conduction bands of TiO_2 NPs, making them promising photocatalysts [17]. However, bare TiO_2 NPs exhibit poor photocatalytic activity due to their high bandgap energy (3.2 eV), which restricts light absorption in the ultraviolet (UV) region (3%–5% of sunlight) [18, 19] and causes rapid recombination of photogenerated electrons (e^-) and holes (h^+). To address this issue, TiO_2 NPs are doped with various dopants via approaches such as ionic liquid (IL)-assisted hydrothermal synthesis, hydrothermal synthesis, sol–gel method, combustion, and co-precipitation [20, 21]. Room-temperature ILs have unique properties such as very low melting point, low vapor pressure, enhanced chemical and thermal stability, nonvolatility, easy solubility in various organic and inorganic solvents, high electrical conductivity, high viscosity, and low density [22, 23]. Interaction of ILs with TiO_2 NPs results in the nucleation and growth of NPs, which helps in controlling the NPs morphology. ILs have several properties, which make them ideal for synthesizing inorganic and inorganic–organic hybrid materials [24]. They are also used as additional solvent materials and surface-directing agents (SDAs) for synthesizing nanocomposites (NCs) via hydrothermal synthesis, based on these advantageous of ILs in hydrothermal synthesis, NCs prepared via IL-assisted hydrothermal synthesis are considered the most protuberant towards photocatalytic and antibacterial activities [25].

Herein, novel Ru/TiO_2 NCs were synthesized via IL-assisted hydrothermal method and conventional hydrothermal method. Different concentrations of ruthenium (III) nitrate were used to synthesize these NCs and to compare their physical and chemical properties towards photocatalytic degradation and antibacterial activities. The role of IL and reaction mechanism has been emphasized in the present work.

Experimental

Materials

Titanium (IV) isopropoxide, ruthenium(III) nitrate, ethanol, sodium hydroxide (NaOH), and Evans blue dye were purchased from Sigma Aldrich (Bommasandra, Jigani Link Road, Industrial Area, Anekal Taluk, Bangalore 560010, Karnataka, India). The 1-butyl-2,3-dimethylimidazolium tetrafluoroborate IL was produced in a lab [26]. Double distilled H_2O was employed for all experimental studies.

Syntheses of TiO_2 NPs and Ru/TiO_2 NCs via hydrothermal method and IL-assisted hydrothermal method

25 mL of titanium isopropoxide was added to 20 mL of ethanol and 20 mL of distilled water, and the mixture was acidified with 2–3 drops of HCl. The resulting mixture was agitated at 660 r/min, followed by sonication for 20 min. The homogeneous solution was then transferred to an autoclave and subjected to hydrothermal treatment for an incubation period of 24 h at 130 °C. After 24 h of incubation, the autoclave was allowed to cool to room temperature, and the resulting precipitate was washed, filtered, and calcined at 400 °C for 2 h to obtain pure white TiO_2 NPs. TiO_2 NPs were synthesized via IL-assisted hydrothermal method by following conventional hydrothermal procedures and post-calcination processes except for the first step. 25 mL of titanium isopropoxide was mixed with 20mL of ethanol and 20 mL of distilled water, the mixture was acidified with two–three drops of HCl and 2–3 mL of IL was added as the SDA to prevent agglomeration and aggregation during synthesis. Ru incorporated TiO_2 NPs (Ru/TiO_2 NCs) were prepared using same synthesis and post-calcination processes, except for the first step. Different concentrations (0.1, 0.2, 0.3, and 0.4 wt%) of ruthenium(III) nitrate were mixed with a fixed volume of titanium isopropoxide via hydrothermal method; the as-synthesized products were labeled R_1TH (0.1-wt% Ru), R_2TH (0.2-wt% Ru), R_3TH (0.3-wt% Ru), and R_4TH (0.4-wt% Ru) (Fig. 1 and Table1). The composition of four samples containing varied ruthenium(III) nitrate concentrations synthesized via IL-assisted hydrothermal method, namely R_1TL (0.1-wt% Ru), R_2TL (0.2-wt% Ru), R_3TL (0.3-wt% Ru), and R_4TL (0.4-wt% Ru),are shown in Fig. 1 and Table 2. All the samples were finely ground and stored separately in different sample bottles for subsequent studies. Figure 2 shows the physical morphology of the synthesized Ru/TiO_2 NCs.

Photocatalytic degradation of dyes

The dye was subjected to photocatalytic decay in a batch reactor (150 mm × 75 mm) via illumination

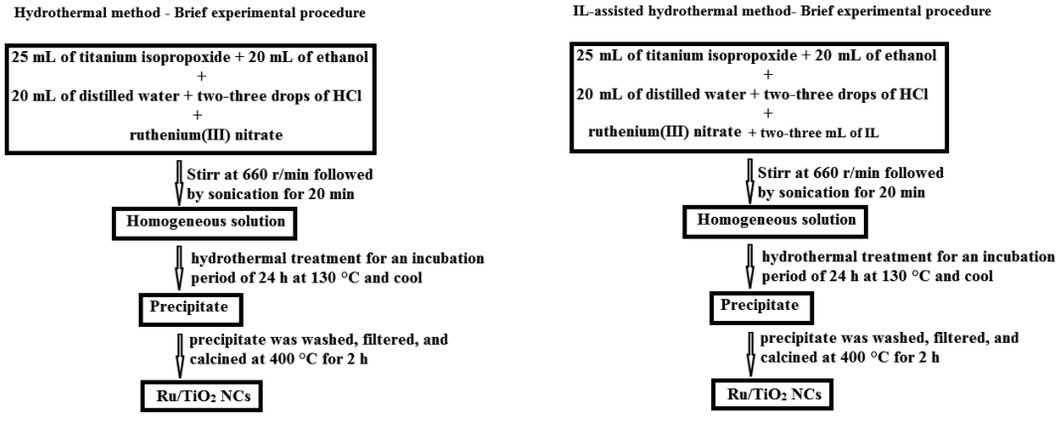

Fig. 1 Flow chart of the synthesis of Ru-doped TiO_2 NCs via hydrothermal method and IL-assisted hydrothermal method.

Table 1 Chemical composition of Ru/TiO_2 NCs synthesized via hydrothermal method

Sample No.	Chemical composition	Sample name
1	Titanium isopropoxide + 20-mL ethanol + 20-mL distilled water + 2–3-drop HCl + 0.1-wt% $Ru(NO_3)_3$	R_1TH
2	Titanium isopropoxide + 20-mL ethanol + 20-mL distilled water + 2–3-drop HCl + 0.2-wt% $Ru(NO_3)_3$	R_2TH
3	Titanium isopropoxide + 20-mL ethanol + 20-mL distilled water + 2–3-drop HCl + 0.3-wt% $Ru(NO_3)_3$	R_3TH
4	Titanium isopropoxide + 20-mL ethanol + 20-mL distilled water + 2–3-drop HCl + 0.4-wt% $Ru(NO_3)_3$	R_4TH

Table 2 Chemical composition of Ru/TiO_2 NCs synthesized via IL-assisted hydrothermal method

Sample No.	Chemical composition	Sample name
1	Titanium isopropoxide + 20-mL ethanol + 20-mL distilled water + 2–3-drop HCl + two–three mL of IL + 0.1-wt% $Ru(NO_3)_3$	R_1TL
2	Titanium isopropoxide + 20-mL ethanol + 20-mL distilled water + 2–3-drop HCl + two–three mL of IL + 0.2-wt% $Ru(NO_3)_3$	R_2TL
3	Titanium isopropoxide + 20-mL ethanol + 20-mL distilled water + 2–3-drop HCl + two–three mL of IL + 0.3-wt% $Ru(NO_3)_3$	R_3TL
4	Titanium isopropoxide + 20-mL ethanol + 20-mL distilled water + 2–3-drop HCl + two–three mL of IL + 0.4-wt% $Ru(NO_3)_3$	R_4TL

Fig. 2 Images of TiO_2 NPs, 0.1-wt% Ru/TiO_2 (R_1TH), 0.2-wt% Ru/TiO_2 (R_2TH), 0.3-wt% Ru/TiO_2 (R_3TH), and 0.4-wt% Ru/TiO_2 (R_4TH) synthesized via hydrothermal method (First line). TiO_2 NPs, 0.1-wt% Ru/TiO_2 (R_1TL), 0.2-wt% Ru/TiO_2 (R_2TL), 0.3-wt% Ru/TiO_2 (R_3TL), and 0.4-wt% Ru/TiO_2 (R_4TL) synthesized via IL-assisted hydrothermal method (Second line).

with natural sunlight (967 $W \cdot m^{-2}$) and UV light (125 $W \cdot m^{-2}$) [17]. Figure 3 shows the experimental setup for the photocatalytic degradation of dye (photocatalytic reactor). 100 mL of dye solution with varying concentrations and pH 3–12 was taken in different aliquots (pH of the reaction mixture was adjusted to the required range using 0.05-M H_2SO_4 and 0.1-N NaOH solutions). Then, different concentration of Ru/TiO_2 NCs were added to these aliquots and stirred using a magnetic stirrer under simultaneous sun and UV light illuminations for 120 min. A standard volume (5 mL) of aliquot slurry was withdrawn at every 30 min and centrifuged at 550 r/min to remove Ru/TiO_2 NCs. The solution absorbance was monitored using an UV–Vis spectrophotometer for determining the magnitude of degradation.

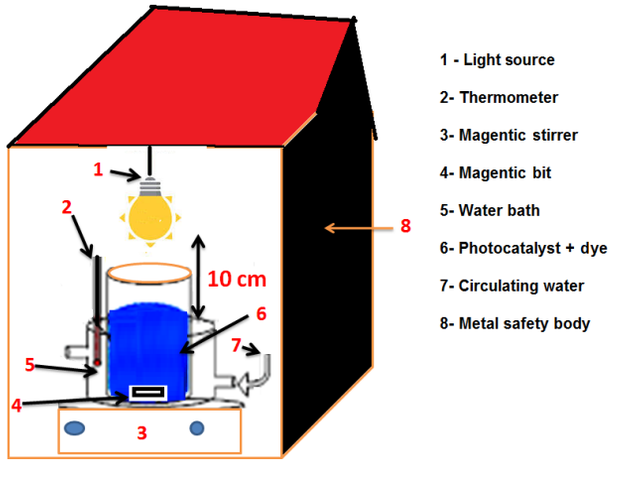

Fig. 3 Batch photocatalytic reactor designed for dye degradation.

Analysis of the antibacterial activity of Ru/TiO_2 NCs

The antibacterial activity of the as-synthesized NCs was analyzed using agar well diffusion test [19], and disk diffusion method was used as the positive control. The antibacterial activities of R_3TH and R_3TL were determined using bacterial strains of *Bacillus* sp., *Escherichia coli*, *Pseudomonas aeruginosa*, *Klebsiella pneumoniae*, *Staphylococcus aureus*, and *Acinetobacter baumannii*. Pure broth cultures of each of these strains were incubated for 24 h and grown as a mat using the spread plate method on the surface of a nutrient agar plate using a sterilized L-shaped glass rod. Subsequently, 6-mm wells were equidistantly created on each plate using a sterile cork borer. Double distilled water was used to disperse 200, 100, 50, and 25 mg/well of both R_3TH and R_3TL to wells 1, 2, 3, and 4, respectively. R_3TH and R_3TL were diluted via serial dilution using the stock solution from the first well. 50 µL of diluted

R_3TH and R_3TL were added to their respective plates. The antibiotic, ampicillin (30 mg/mL, Hi-Media), was used as the positive control in the center of the plate. Double distilled water was used as the negative control in the 5th well. These plates were incubated in a biological oxygen demand (BOD) incubator at 37 °C for 24–36 h, and the antibacterial activity was determined by measuring the diameter of clear circular zones around the bacterial growth after incubation [11].

Characterization

The nanocrystal structure of the prepared NCs was analyzed via powder X-ray diffraction (PXRD), Rigaku II Cu–K_α using a Cu–K_α radiation (λ = 1.5418 Å) operating at 40 kV and 30 mA). The crystallite size was estimated for the maximum intensity peak from the powder diffractogram using Scherrer's equation, The surface morphology and elemental distribution of the samples were investigated using the scanning electron microscopy (SEM) and energy-dispersive X-ray spectroscopy (EDS) spectra obtained using Hitachi 3000 SEM. The HRTEM images of samples were obtained using JEOL JEM 1200 EX at 100 kV. For obtaining the transmission electron microscopy (TEM) images, a dispersion solution containing NCs and 2-propanol was dropped on the carbon grid and vacuum-dried for 24 h. ESCALAB 250 (Thermo-VG Scientific) that used Al–K_α as the excitation source was used to obtain the X-ray photoelectron spectroscopy (XPS) spectra. The UV spectral absorption of NPs dispersed in the aqueous medium was determined using double-beam UV–Vis spectrophotometer (Schimadzu 2600). Micromeritics Tristar II surface area analyzer was used to study the N_2 desorption–adsorption mechanism for determining the BET surface area. The pH of the reaction media was monitored using a Systronics MK VI digital pH meter.

Results and Discussion

Powder X-ray diffraction (PXRD)

The composition, crystal structure, and phase purity of the as-synthesized NCs were analyzed via PXRD, for which the NCs were calcined at 400 °C for 2 h. Figures 4(a) and 4(b) show the PXRD diffraction patterns of bare TiO_2 NPs and different concentrations of Ru/TiO_2 NCs synthesized via the hydrothermal method and IL-assisted hydrothermal method, respectively. Figure 4(a) shows prominent peaks at 25.30°, 37.81°, 48.11°, 53.80°, 55.10°, 62.80°, 68.61°, 70.31°, and 74.91°, corresponding to the (101), (004), (200), (105), (211), (204), (116), (220), and (215) reflection planes, respectively. These findings confirmed the existence of well-crystallized TiO_2 with a pure anatase phase (JCPDS file 21-1272) without any rutile or brookite phases. Ru/TiO_2 NCs did not show any additional peaks for Ru, and no new phase formation was observed possibly because of low Ru concentration detected by PXRD. The average crystallite size of bare TiO_2 NPs and Ru/TiO_2 NCs were calculated using the Eq. (1) (Debye–Scherrer equation) of the anatase-phase (101) diffraction peak as follows:

$$D = \frac{k\lambda}{\beta\cos\theta} \quad (1)$$

where D is the average crystallite size of the NP, k is the crystallite shape factor (0.89), λ is the Cu X-ray wavelength (0.540 6 nm), θ is the diffraction angle for the anatase-phase (101) peak, and β is the full width at half maxima. Table 3 shows the computed

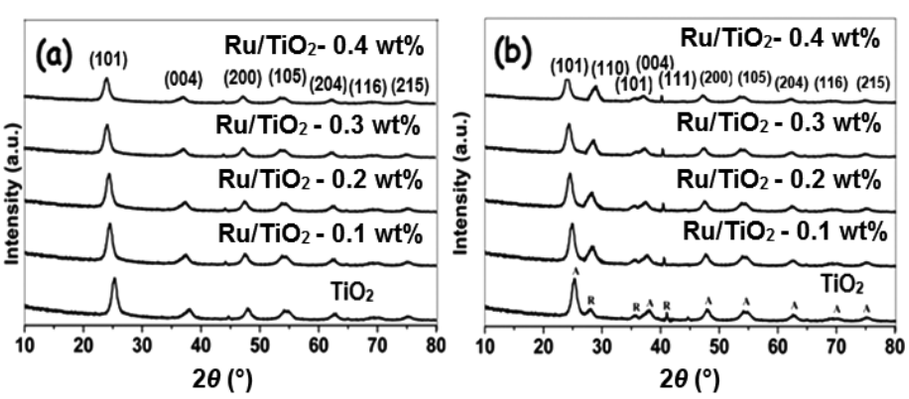

Fig. 4 PXRD patterns of bare TiO_2 NPs and Ru/TiO_2 NCs synthesized using the **(a)** hydrothermal and **(b)** IL-assisted hydrothermal methods.

Table 3 Nanocrystalline sizes of the bare TiO_2 NPs and Ru/TiO_2 NCs synthesized using the hydrothermal method and IL-assisted hydrothermal method

Name of the photocatalyst	Ru content in TiO_2 structure (wt%)	Crystalline size (nm) using hydrothermal method	Crystalline size (nm) using IL-assisted hydrothermal method
TiO_2 NPs	—	17.26 for (101) anatase	17.30 for (101) anatase 18.10 for (110) rutile
Ru/TiO_2 NCs	0.1	17.10 for (101) anatase	17.28 for (101) anatase 18.21 for (110) rutile
	0.2	17.11 for (101) anatase	17.26 for (101) anatase 18.24 for (110) rutile
	0.3	17.12 for (101) anatase	17.24 for (101) anatase 18.27 for (110) rutile
	0.4	17. 21 for (101) anatase	17.21 for (101) anatase 18.30 for (110) rutile

average nanocrystallite sizes for bare TiO_2 NPs, 0.1-wt% Ru/TiO_2 NCs, 0.2-wt% Ru/TiO_2 NCs, 0.3-wt% Ru/TiO_2 NCs, and 0.4-wt% Ru/TiO_2 NCs, which do not show any considerable changes in the nanocrystallite sizes. The peaks shifted toward lower 2θ values when Ru was doped in the TiO_2 nanostructure, and the lattice constants and inter planar distance (d-spacing) increased due to a slight increase in the effective ionic radius of Ru^{4+} (0.062 nm) than that of Ti^{4+} (0.060 5 nm) in the anatase structure. The PXRD peaks shifted toward lower 2θ values due to increased d-spacing of the anatase nanostructure. The PXRD patterns of bare TiO_2 NPs and Ru/TiO_2 NCs synthesized via the IL-assisted hydrothermal method showed peaks at 25.31°, 37.80°, 48.10°, 53.79°, 55.10°, 62.80°, 68.60°, 70.30°, and 74.90°, corresponding to the (101), (004), (200), (105), (211), (204), (116), (220), and (215) reflection planes, respectively (Fig. 4(b)); this confirmed the presence of nanocrystalline anatase-phase TiO_2. The peaks at 27.38°, 36.08°, and 41.3° correspond to the (110), (101), and (111) reflection planes, respectively for the rutile-phase TiO_2. Both rutile and anatase phases were observed due to the incorporation of IL, which served as the SDA in synthesizing TiO_2 and Ru/TiO_2 NCs using the hydrothermal method. Moreover, the intensities of the anatase and rutile phases slightly decreased as the concentration of Ru increased in the TiO_2 structure (0.1–0.4 wt%). These observations suggested that Ru doping inhibited the growth of TiO_2 nanocrystals because of the formation of strong interaction among Ru and TiO_2 and Ru–O–Ti bonds. The utilization of IL as an SDA in hydrothermal synthesis facilitated the formation of a self-assembling template, which further reduced the agglomeration and aggregation of NPs during the synthesis of NCs. The effects of phase purity, surface morphology (shape), and crystalline sizes of TiO_2 NPs on the properties and performances of Ru/TiO_2 NCs have not been extensively studied, and several contradictory results/statements have been reported in some publications [7–10], e.g., influence of TiO_2 phase composition on the photocatalysis. Some studies showed that the photocatalytic activity of anatase-phase TiO_2 was considerably higher than that of the rutile-phase TiO_2. However, a few studies have shown that TiO_2 with mixed phases (both anatase and rutile phases) showed higher photocatalytic activities due to the synergistic effect of both the phases. These observations indicate the reason for enhanced photocatalytic activity of Ru/TiO_2 NCs synthesized via IL-assisted hydrothermal method compared with those synthesized via the hydrothermal method. The average crystallite size of bare TiO_2 NPs and 0.1-wt% Ru/TiO_2 NCs, 0.2-wt% Ru/TiO_2 NCs, 0.3-wt% Ru/TiO_2 NCs, and 0.4-wt% Ru/TiO_2 NCs were calculated using the Debye–Scherrer equation of the anatase-phase (101) and rutile-phase (110) peaks (Table 3).

Role of ILs in the hydrothermal synthesis of TiO_2 NPs and Ru/TiO_2 NCs

The synthesis of NCs using the hydrothermal method is posed with some issues [22] such as no control over NPs aggregation and difficulty in fine-tuning the surface properties of NCs. To overcome these drawbacks, 1-butyl-2,3-dimethylimidazolium tetrafluoroborate was used as the IL for the hydrothermal synthesis of NCs. ILs primarily function as SDAs (surfactants) for synthesizing inorganic NCs, hindering the agglomeration of NCs. ILs are also an excellent media for synthesizing TiO_2 NPs and Ru/TiO_2 NCs. The shape and size of TiO_2 NPs and Ru/TiO_2 NCs can be regulated by fine-tuning the composition of reactants. The cationic and anionic groups in ILs adsorbed on the TiO_2 NP surface [26] and prevented the aggregation of anatase-

and rutile-phase NCs. The cationic group in the ILs adsorbed on the NCs and acted as a protective shell, further minimizing the random aggregation of anatase NCs and influencing the nucleation of rutile NCs [22]. Herein, the reaction temperature, pH, and reactant concentration played a major role in the phase transformation of NCs and modifying the shape and size of anatase and rutile NCs. Moreover, feasible phases were proposed for synthesizingTiO_2 and Ru/TiO_2 NCs and their phase transformation from anatase to rutile during IL-assisted hydrothermal synthesis was proposed.

Phase 1: Hydrolysis of Ti precursor. During this phase, ligands around Ti atoms were substituted by OH^- groups due to the attack of H_2O molecules. Thus, Ti-oxo bridges were formed and served as the monomers for the nucleation and crystal growth of NCs.

Phase 2: Nucleation of anatase-phase NCs. Due to the rapid hydrolysis of Ti precursors, the concentration of Ti-oxo species substantially increased rapidly. Moreover, the degree of super saturation exceeded the energy barrier for nucleation, creating a nucleation burst, which rapidly reduced the concentration of Ti-oxo species and formed anatase-phase NCs.

Phase 3: Nucleation of rutile-phase NCs. Rutile-phase NCs aggregated after the anatase-phase NCs in this phase due to nucleation burst, thereby forming different structures at the interfaces between NCs of both the anatase phases. Some these interface structures were identical to the rutile structures, which served as the nucleation sites for the formation of rutile-phase NCs. Subsequently, the aggregated anatase-phase NCs irreversibly transform into rutile-phase NCs.

Phase 4: Ostwald ripening. Both the anatase and rutile phases of TiO_2 NCs were involved in chemical reactions. The equilibrium constants between Ti-oxo species varied with the phase, shape, and size of TiO_2 NCs due to their different chemical potentials. Consequently, NCs with lower chemical potentials increased, benefiting from the sacrifice of NCs with higher chemical potentials.

BET surface area, quantum yield, and bandgap energy of the as-prepared nanomaterials

Table 4 shows the BET surface areas of bare TiO_2 NPs and R_1TH, R_2TH, R_3TH, and R_4TH as well as bare TiO_2 NPs and R_1TL, R_2TL, R_3TL, and R_4TL. The N_2 adsorption–desorption isotherms and Barrett–Joyner–Halenda (BJH) pore size distribution plots of the prepared R_3TH and R_3TL are shown in Figs. 5(a), 5(b), 6(a), and 6(b), respectively. The BET surface areas and BJH plots of other samples are not included herein. The BET plots of R_3TH and R_3TL showed a typical type-IV hysteresis loop in line with the IUPAC, revealing that 0.3-wt% Ru/TiO_2 NCs have a higher BET surface than bare TiO_2 NPs. Moreover, R_3TL had a higher surface area than R_3TH. The quantum efficiencies of the synthesized photocatalysts were determined and compared, which revealed that R_3TL had the highest quantum efficiency among all the synthesized nanomaterials; thus, it is considered the most ideal photocatalyst for photocatalytic dye absorption. The optical properties

Table 4 BET surface area, quantum yield, and bandgap energy of bare TiO_2 NPs and Ru/TiO_2 NCs synthesized using the hydrothermal method and IL-assisted hydrothermal methods

Method	Samples	BET surface area ($m^2 \cdot g^{-1}$)	Quantum yield	Bandgap (eV)
Hydrothermal method	TiO_2	35.5	0.20	3.25
	R_1TH	42.4	0.23	3.19
	R_2TH	44.8	0.25	3.00
	R_3TH	59.5	0.30	2.73
	R_4TH	48.1	0.31	2.68
IL-assisted hydrothermal method	TiO_2	42.3	0.22	3.20
	R_1TL	48.2	0.25	3.10
	R_2TL	52.4	0.28	2.90
	R_3TL	89.1	0.32	2.82
	R_4TL	54.1	0.29	2.78

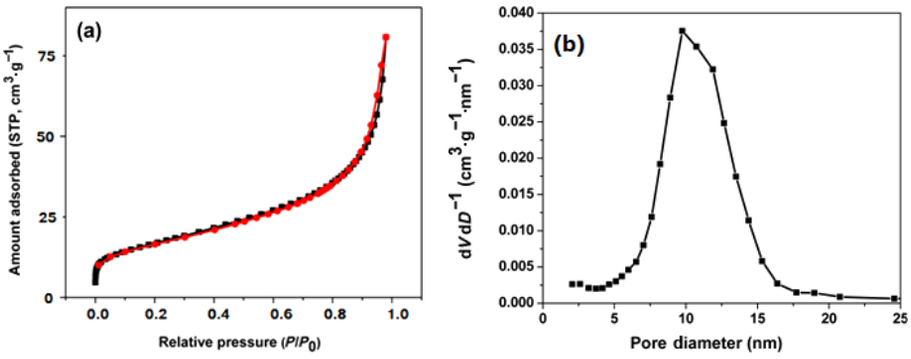

Fig. 5 (a) N_2 gas adsorption–desorption isotherms of the synthesized photocatalysts. **(b)** BJH pore size distribution curves of R_3TH.

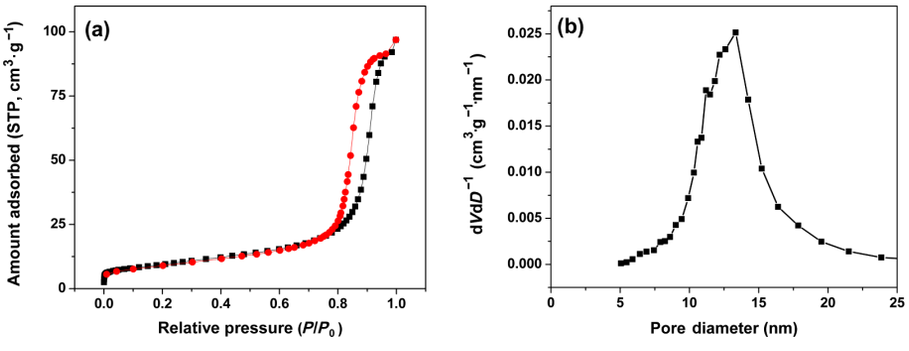

Fig. 6 (a) N_2 gas adsorption–desorption isotherms of the synthesized photocatalysts. **(b)** BJH pore size distribution curves of R_3TL.

and bandgap energies of all NCs were quantified via UV–Vis spectrophotometer at 200–800 nm and room temperature (Fig. 7). The bandgap energies were calculated from the diffuse reflectance spectra using the Kubelka–Munk function (Table 4). Bare TiO_2 NPs exhibited a bandgap energy of ~ 3.20–3.25 eV. Upon Ru doping, the bandgap energies of Ru/TiO_2 NCs decreased to 2.70 eV and the light absorption of the heterojunction-containing NC increased. UV–Vis spectroscopy of Ru/TiO_2 NCs showed a redshift in the optical response toward the visible region, which decreased the bandgap energy and increased light absorption in the visible spectrum. These findings

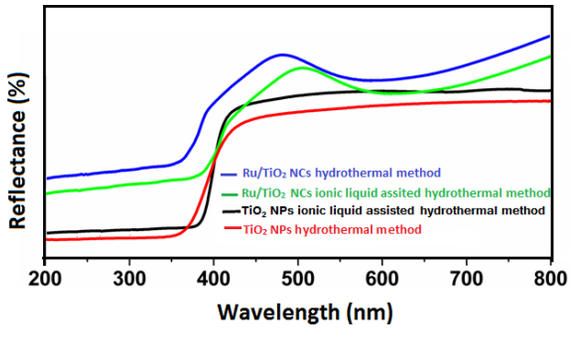

Fig. 7 UV–Vis spectra of TiO_2 NPs and Ru/TiO_2 NCs synthesized using the hydrothermal method and IL-assisted hydrothermal method.

suggest that R_3TL is an ideal catalyst that exhibits enhanced photocatalytic degradation and antibacterial activities compared with other NCs.

Photoluminescence spectroscopy

Photoluminescence (PL) spectroscopy can be performed for the probing of electronic structure and analyzing the effect of Ru doping into TiO_2 nanocrystalline structure. Low-temperature PL spectroscopy was performed by exciting bare TiO_2 NPs and Ru/TiO_2 NCs synthesized via hydrothermal and IL-assisted hydrothermal methods under 350-nm UV irradiation. Figure 8 shows the presence of a strong emission peak at ~ 455 nm [14] in the emission spectra of all the synthesized samples. Pristine TiO_2 NPs synthesized using hydrothermal and IL-assisted hydrothermal methods exhibited the highest relative intensity compared with other samples. The excited electrons from the conduction band and holes in the valance band recombine rapidly in pristine TiO_2 NPs. The low spectral intensities of Ru/TiO_2 NCs indicated that Ru doping minimized the recombination speed of charge carriers, which enhanced photocatalytic and surface properties of NCs than the bare TiO_2 NPs. A comparison of relative PL intensities of the NCs synthesizing using the two hydrothermal methods

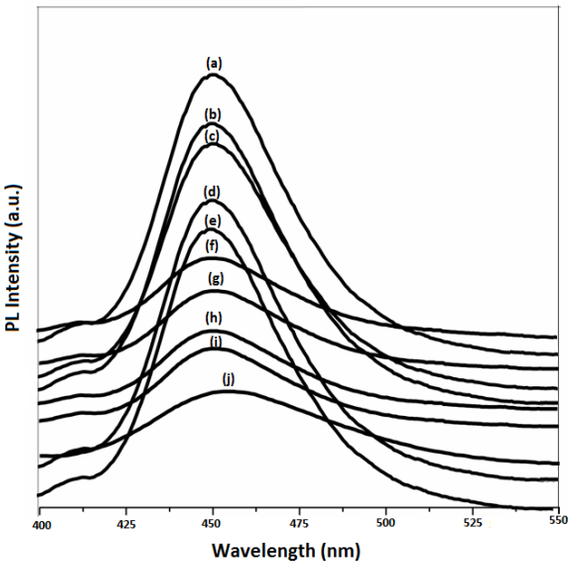

Fig. 8 PL spectra of bare TiO_2NPs synthesized using **(a)** hydrothermal method and **(b)** IL-assisted hydrothermal method, **(c)** R_1TH, **(d)** R_2TH, **(e)** R_3TH, **(f)** R_4TH, **(g)** R_1TL, **(h)** R_2TL, **(i)** R_3TL, and **(j)** R_4TL.

revealed slower electron–hole recombination in those synthesized via IL-assisted hydrothermal method. As a result, these NCs exhibited enhanced photocatalytic and antibacterial activities. Moreover, the concentrations of Ru in the TiO_2 nanostructure regulated the electron–hole recombination speed. R_3TH showed the lowest relative intensity of emission because the addition of 0.3-wt% Ru into TiO_2 nanocrystalline structure effectively restrained the overlapping of photoexcited electrons and holes. When small amounts of Ru (0.1 and 0.2 wt%) was added in the TiO_2 nanocrystalline structure, sufficient traps were not present and higher over lapping electron–hole pairs was higher. When 0.4-wt% Ru was added, both light absorption and electron–hole generation were inhibited [25, 26]. Thus, PL spectroscopy results suggested the formation of donor levels, defect levels, and surface trap states after Ru doping concentration reached 0.3 wt%; these defects functioned as effective charge recombination pathways [21].

Photocatalytic degradation of Evans blue dye

To evaluate the photocatalytic efficiencies of the as-synthesized nanomaterials toward the Evans blue dye, their photocatalytic activities were determined (P-25 Degusa TiO_2, R_1TH, R_2TH, R_3TH, R_4TH, R_1TL, R_2TL, R_3TL, and R_4TL); the corresponding results are shown in Fig. 9. A comparison between the synthesized nanomaterials revealed that bare TiO_2

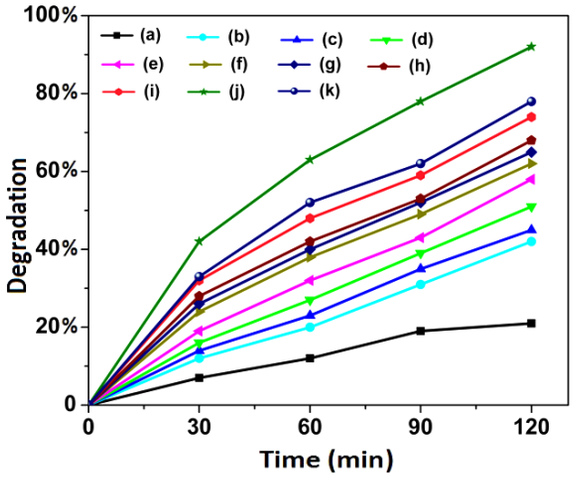

Fig. 9 Photocatalytic degradation of Evans blue dye by **(a)** commercial TiO_2 (Degussa P-25), **(b)** bare TiO_2 NPs using the hydrothermal method, **(c)** R_1TH, **(d)** R_2TH, **(e)** R_3TH, **(f)** R_4TH, and **(g)** TiO_2 NPs synthesized via IL-assisted hydrothermal method, **(h)** R_1TL, **(i)** R_2TL, **(j)** R_3TL, and **(k)** R_4TL.

NPs synthesized using the hydrothermal and IL-assisted hydrothermal methods have exhibited enhanced photocatalytic degradation than the commercially available TiO_2 powder (DegussaP-25).This indicates the importance of nanomaterials toward photocatalytic activity than commercially available bulk materials. In addition, R_1TH, R_2TH, R_3TH, R_4TH, R_1TL, R_2TL, R_3TL, and R_4TL exhibited better photocatalytic activities than bare TiO_2 NPs, indicating that Ru/TiO_2 NCs are promising photocatalysts. Furthermore, a comparison of the photocatalytic degradation between the nanomaterials synthesized from hydrothermal and IL-assisted hydrothermal methods proved that the nanomaterials synthesized from IL-assisted hydrothermal method showed enhanced photocatalytic activities and indicated that the importance of ILs in hydrothermal method. The concentration of Ru in the TiO_2 nanocrystalline structure considerably enhanced the photocatalytic efficiency. 0.3-wt% Ru/TiO_2 NCs synthesized using the IL-assisted hydrothermal method showed the highest photocatalytic degradation (Evans blue dye removal of 97.22% within 2 h under visible and UV light irradiation).

Effects of UV–Vis irradiation on the photocatalytic activity

The effect of UV and visible light intensities on the photocatalytic degradation of Evans blue dye by R_3TL was analyzed, the corresponding results are shown in Fig. 10. R_3TL removed 85% and 95.5%

Evans blue dye when exposed to UV and visible light, respectively. R_3TL exhibited enhanced photocatalytic activity under visible light illumination due to its unique physical and chemical properties such as higher bandgap energy, quantum efficiency, and surface area and enhanced surface morphology (Tables 3 and 4; Fig. 11). The bandgap energy of an ideal photocatalyst should be 1.23 eV < E_g< 3.3 eV or < 3 eV [13]. This allows light absorption to extend into the visible region and efficiently use solar energy. R_3TL exhibited bandgap energy of 2.82 eV, which is a possible cause of its enhanced photocatalytic activity. Moreover, a promising photocatalyst should efficiently separate photogenerated electrons and holes and transport them to their reactive sites to reduce the electron–hole pair recombination. Correspondingly, R_3TL showed an appropriate bandgap energy (2.82 eV), thereby achieving a wide electron–hole separation (Fig. 11). When the energy of incident light is higher than the bandgap energy of R_3TL, electrons were excited from the valence band (VB) to the conduction bandgap (CB) of TiO_2. Then, the electrons in the CB of TiO_2 transferred to the CB of Ru, minimizing the electron–hole pair recombination and enhancing the photocatalytic efficiency of R_3TL. Holes form the VB of TiO_2 oxidized the Evans blue dye adsorbed on the photocatalyst surface. Thus, the nanocomposite formed between TiO_2 and Ru efficiently separated the photoexcited charge carriers and reduced charge recombination, thereby improving the photocatalytic activity of R_3TL compared with bare TiO_2 NPs and NCs. When higher amounts of Ru were added to the TiO_2 nanocrystalline structure, the corresponding light absorption from TiO_2 decreased and inhibited the generation of electron–hole pairs in the TiO_2 structure. This phenomenon may have primarily cause a decrease in the photocatalytic activity of R_3TL NCs with high Ru contents. In the case of bare TiO_2 NPs, most of these electron–hole pairs rapidly recombined and decreased their photocatalytic activity.

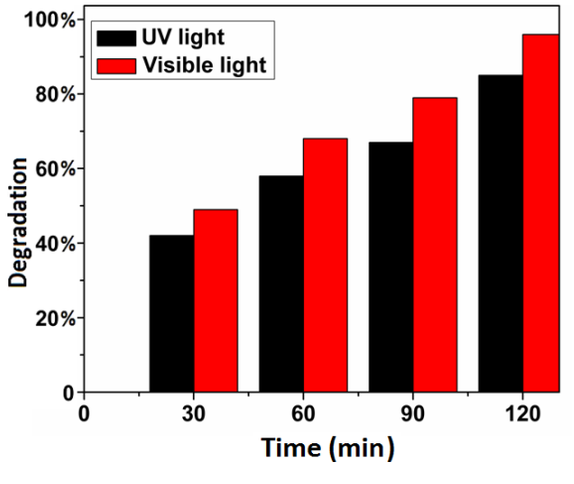

Fig. 10 Effects of illumination with different light sources on the photocatalytic degradation of Evans blue dye by R3TL.

Effect of illumination intensities on the photocatalytic degradation of Evans blue dye

The photocatalytic degradation of Evans blue dye was evaluated under three light illumination intensities (Fig. 12). The first experiment was conducted in the dark at room temperature by keeping all the experimental parameters like catalytic load, pH, dye concentration, and temperature were constant. The Evans blue dye was negligibly degraded, indicating the importance of light illumination during degradation. In contrast, the Evans blue dye markedly degraded under a light source (Xe arc lamps with intensities of 200 and 400 W). Slight photocatalytic degradation (~ 33%) was observed at 200 W, whereas enhanced photocatalytic degradation of ~ 50% was

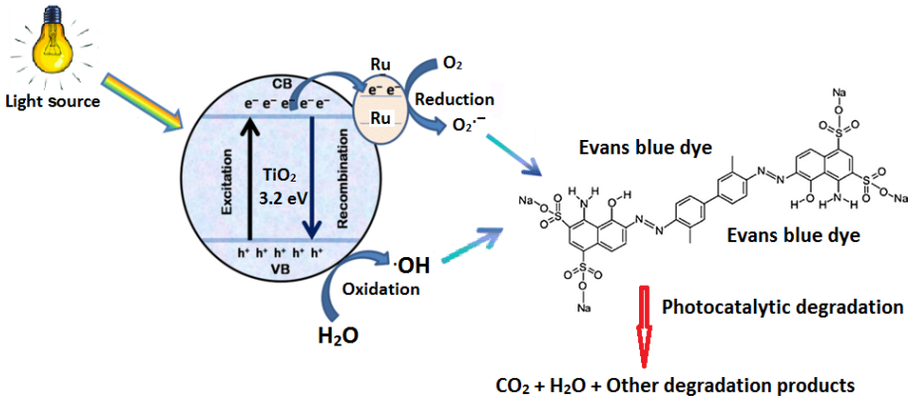

Fig. 11 Photogenerated electron–hole transportation in R3TL NCs for photocatalysis.

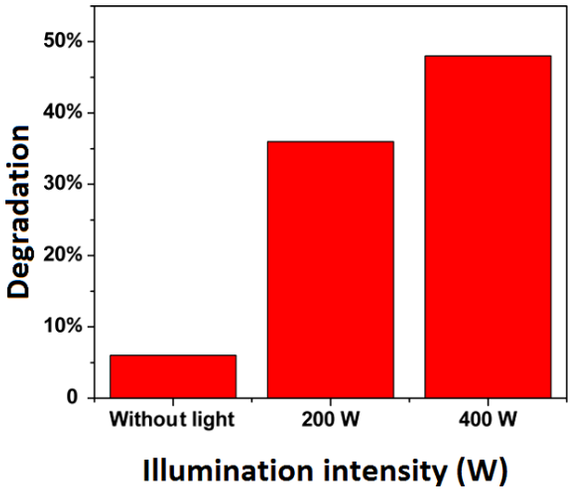

Fig. 12 Influence of illumination intensities on the photocatalytic decay of Evans blue dye by R_3TL (catalytic load = 0.4 g/100 mL, dye concentration = 5 mg/L, and duration = 30 min).

observed at 400 W. This is because the number of incident photons increased with the illumination intensity, thereby increasing the number of conduction band electrons and enhancing the photocatalytic degradation of the dye.

Additional characterization of R_3TL

Given that R_3TL exhibited the highest surface area and superior photocatalytic activity among the samples studied, additional comprehensive characterization was performed to further elucidate its key physical and chemical properties.

X-ray photoelectron spectroscopy (XPS)

Figure 13 shows the XPS results, wherein the chemical oxidation states of Ru, Ti, and O in R_3TL can be observed. Figure 13(a) shows the Ti 2p XPS spectrum, wherein Ti $2p_{3/2}$ and Ti $2p_{1/2}$ peaks with binding energies of 457.8 and 465.7 eV, respectively, were observed, corresponding to Ti^{4+} [10]. Figure 13(b) shows the O 1s XPS spectrum, where in the peak centered at 528.9 eV can be attributed to the incidence of oxygen in the TiO_2 lattice. The adjacent peak at 532.8 eV indicated the presence of surface hydroxide species, which enhanced the photocatalytic degradation of Evans blue dye [16]. The C 1s and Ru 3d XPS spectra of R_3TL regions (Fig. 13(c)) showed peaks at 280.94 and 286.95 eV, assigned to Ru ($3d_{5/2}$), and Ru ($3d_{3/2}$), respectively [25]. The XPS survey spectrum also (Fig. 13(d) shows the existence of Ru, Ti, and O.

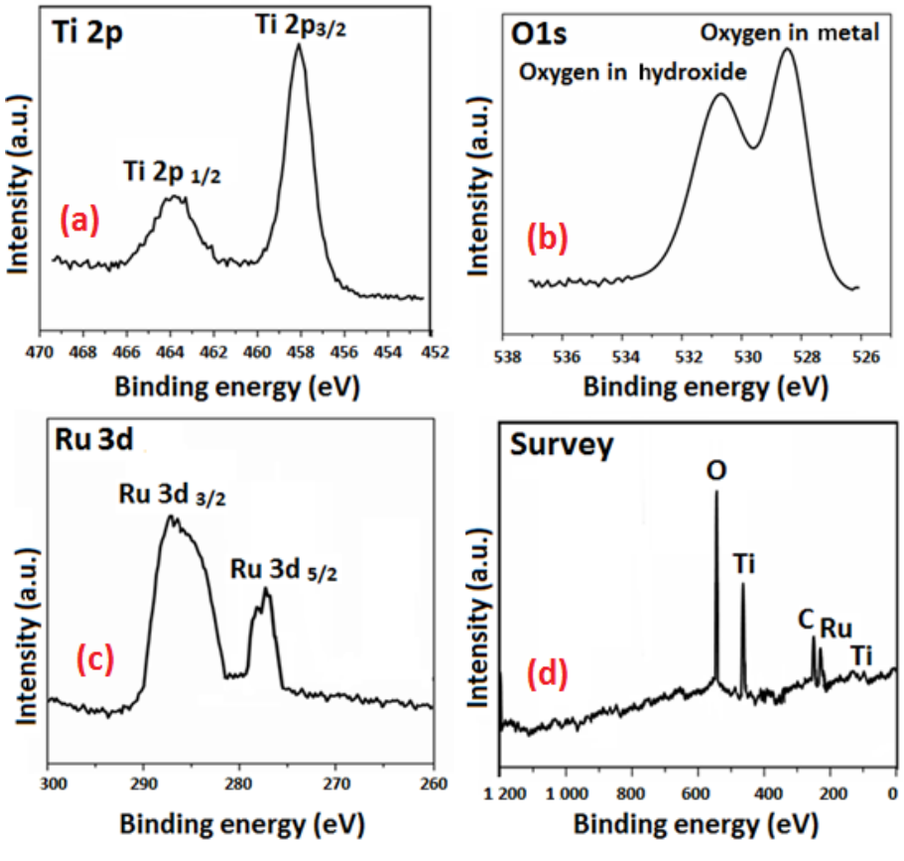

Fig. 13 XPS spectra of **(a)** Ti 2p, **(b)** O 1s, **(c)** Ru 3d regions, and **(d)** broad spectrum of R_3TL.

Surface morphology analysis via SEM

Figures 14(a) and 14(c) show the surface morphologies of R_3TH and R_3TL, respectively. The SEM images of R_3TH (Fig. 14(a)) shows irregularly shaped particles that aggregated to form crystals during the synthesis of these NCs. 1-butyl-2,3-dimethylimidazolium tetrafluoroborate acted as the SDA and formed a self-assembling template during NC synthesis, inhibiting particle collision due to a high energy barrier as well as minimizing the aggregation and agglomeration of R_3TL. These findings indicated that the morphology of NCs can be controlled. R_3TL exhibited a porous and highly voluminous cage-like network with abundant voids (green arrow in Fig. 14(c)), which increased the surface area and enhanced its photocatalytic activity compared with R_3TH. SEM results also clarified that ILs are crucial for inhibiting agglomeration during hydrothermal synthesis.The ILs can act as self-assembling templates, and the anionic group of the IL, i.e., tetrafluoroborate, preferentially mixed with H_2O molecules in the solution via hydrogen bonding owing to its enhanced hydrophilicity [4]. The cationic group of the IL, i.e., 1-butyl-2,3-dimethylimidazolium ring, arrayed in the opposite direction and accumulated possibly via various intermolecular forces between the imidazolium rings [7]. As the IL formed a self-assembling template, it successfully participated in the hydrothermal reaction and minimized the collision and agglomeration of particles. As a result,a highly porous structure with a high surface area was formed (R_3TL; Fig. 14(c)). Owing to this morphology, the water adsorption and penetration rate enhanced along with the photocatalytic degradation of Evans blue dye by R_3TL. The elemental composition of R_3TH and R_3TL were analyzed via energy-dispersive X-ray (EDAX) spectroscopy. Figure 14(b) shows the EDAX spectra of R_3TH, confirming the presence of Ru, Ti, and O (the corresponding elemental weightand atomic are shown in Fig. 14(b)). Similarly, Fig. 14(d) shows the EDAX spectra of R_3TL, confirming the presence of Ru, Ti, and O in R_3TL. Figure 14 shows that Ru was successfully inserted into the TiO_2 crystalline structure. The structure of 1-butyl-2,3-dimethylimidazolium tetrafluoroborate is shown in Fig. 15.

Transmission Electron Microscope (TEM)

Figures 16(a) and 17(a) show the low-magnification (50 nm) TEM images of R_3TH and R_3TL, respectively. Figure 16(a) shows uniform growth and aggregation of spherical particles,with anaverage particle size of 40.1 nm. The HRTEM image (Fig. 16(b)) shows interplanar distances (*d*) of 0.35 and 0.24 nm, which are in good agreement with the (101) plane of anatase TiO_2 and the (101) plane of

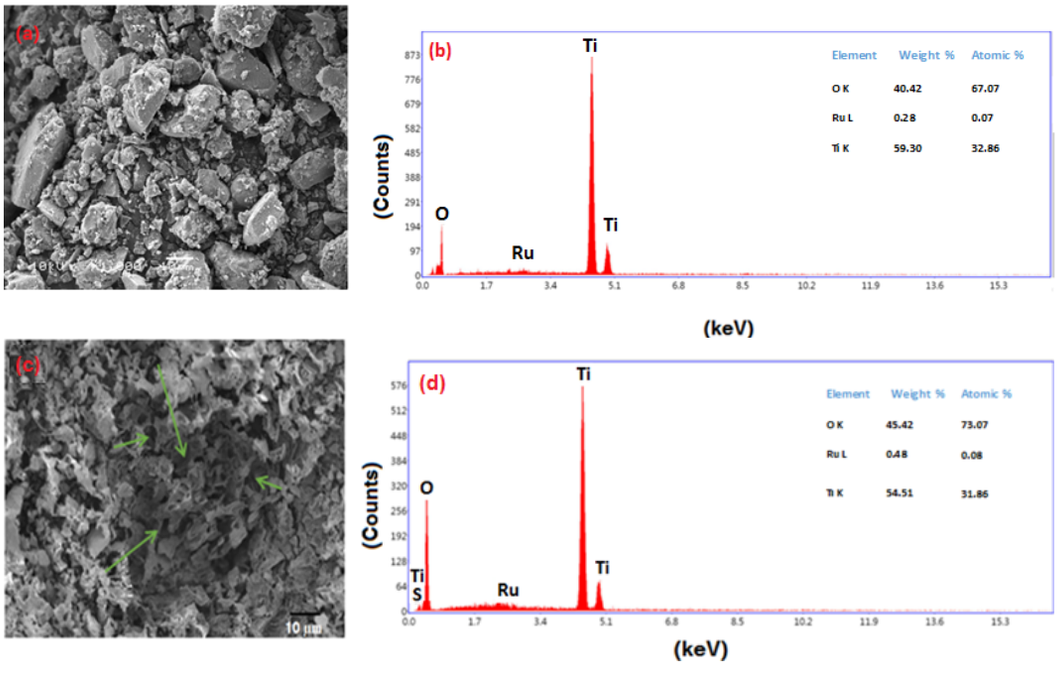

Fig. 14 (a) SEM image and **(b)** EDAX spectrum of R_3TH and **(c)** SEM image, and **(d)** EDAX spectrum of R_3TL (green arrow indicates pore-like structures).

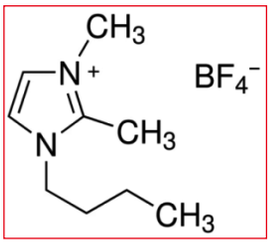

Fig. 15 Chemical structure of 1-butyl-2,3-dimethylimidazolium tetrafluoroborate.

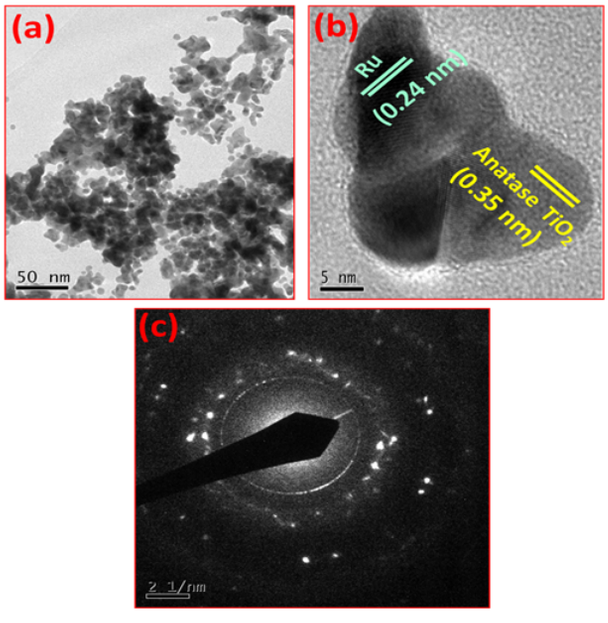

Fig. 16 (a) Low-magnification TEM image, **(b)** HRTEM image, and **(c)** SAED pattern of R_3TH.

Ru, respectively. The corresponding SAED spectrum is shown in Fig. 16(c), which further indicates the existence of Ru in the TiO_2 polycrystalline structure. Figure 17(a) shows uniform growth of spherical particles and their well-dispersed nature with less aggregation.This indicates that IL used in the hydrothermal method minimize aggregation and agglomeration of particles; the average particle size was found to be 38.0 nm. Moreover, the interplanar distances (*d*) were 0.35, 0.32, and 0.24 nm, which agreed well with the (101) plane of anatase TiO_2, (110) plane of rutile TiO_2, and (101) plane of Ru, respectively (Fig. 17(b)). Figure 17(c) shows the SAED spectrum of R_3TL, which further indicated the presence of Ru in the TiO_2 polycrystalline structure.

Thermo gravimetric analysis

The thermal stability of R_3TL was analyzed via thermo gravimetric analysis (TGA); the corresponding TGA plot is shown in Fig. 18. Upon heating the NC from room temperature to 800 °C in

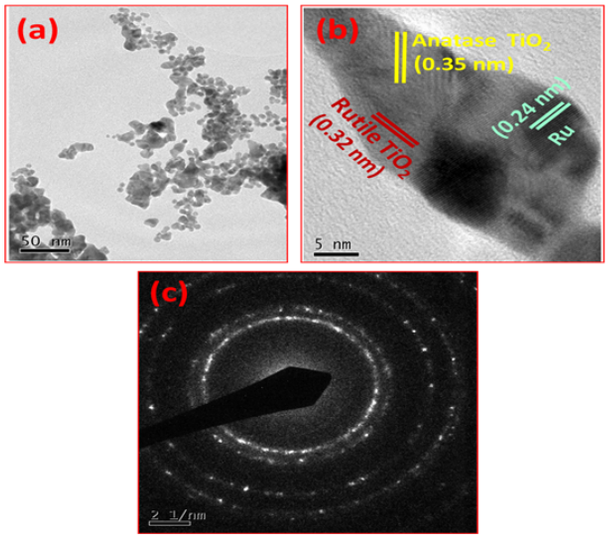

Fig. 17 (a) Low-magnification TEM image, **(b)** HRTEM image, and **(c)** SAED pattern of R_3TL.

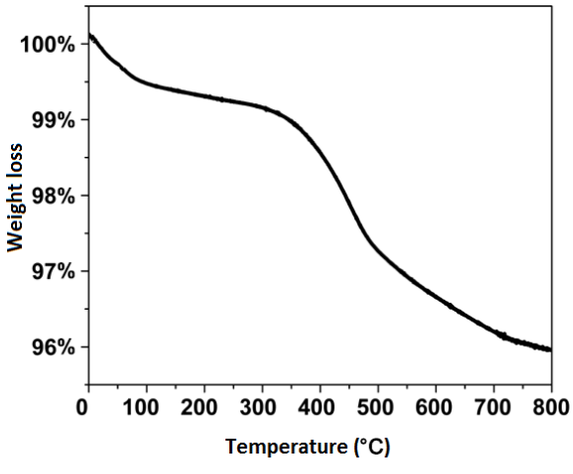

Fig. 18 TGA curve for R_3TL.

air atmosphere, the first weight loss was observed below 100 °C because the H_2O molecules evaporated. This indicated that R_3TL exhibited hydration due to the adsorption of H_2O molecules on its surface. Another weight loss was observed from 100 to 500 °C because of the thermal decomposition of some organic molecules. R_3TL also show organic moiety upon adding ILs during its synthesis. Above 500 °C, almost no weight loss occurred, indicating the high thermal stability of R_3TL. Thus, it can be used in high-temperature applications [8].

Photocatalytic degradation studies of Evans blue dye by R_3TL

Herein, the influence of parameters such as the catalytic load, pH, dye concentration, recyclability/reusability, and the absorption of scavengers on the photocatalytic decay rate of Evans

blue dye by R_3TL was analyzed. The catalytic load (R_3TL) was varied from 0.1 to 0.6 g/100 mL, and the corresponding results are shown in Fig. 19(a). Based on the results, the optimal amount of photocatalyst was deemed 0.4 g/100 mL. The photocatalytic decay of Evans blue dye improved below the optimal load (0.1–0.3 g/100 mL) because abundant reactive sites were present on its surface. In contrast, the photocatalytic decay deteriorated above the optimal load (above 0.4 g/100 mL) because abundant reactive species such as hydroxide and superoxide radicals were not formed due to inhibited penetration of light

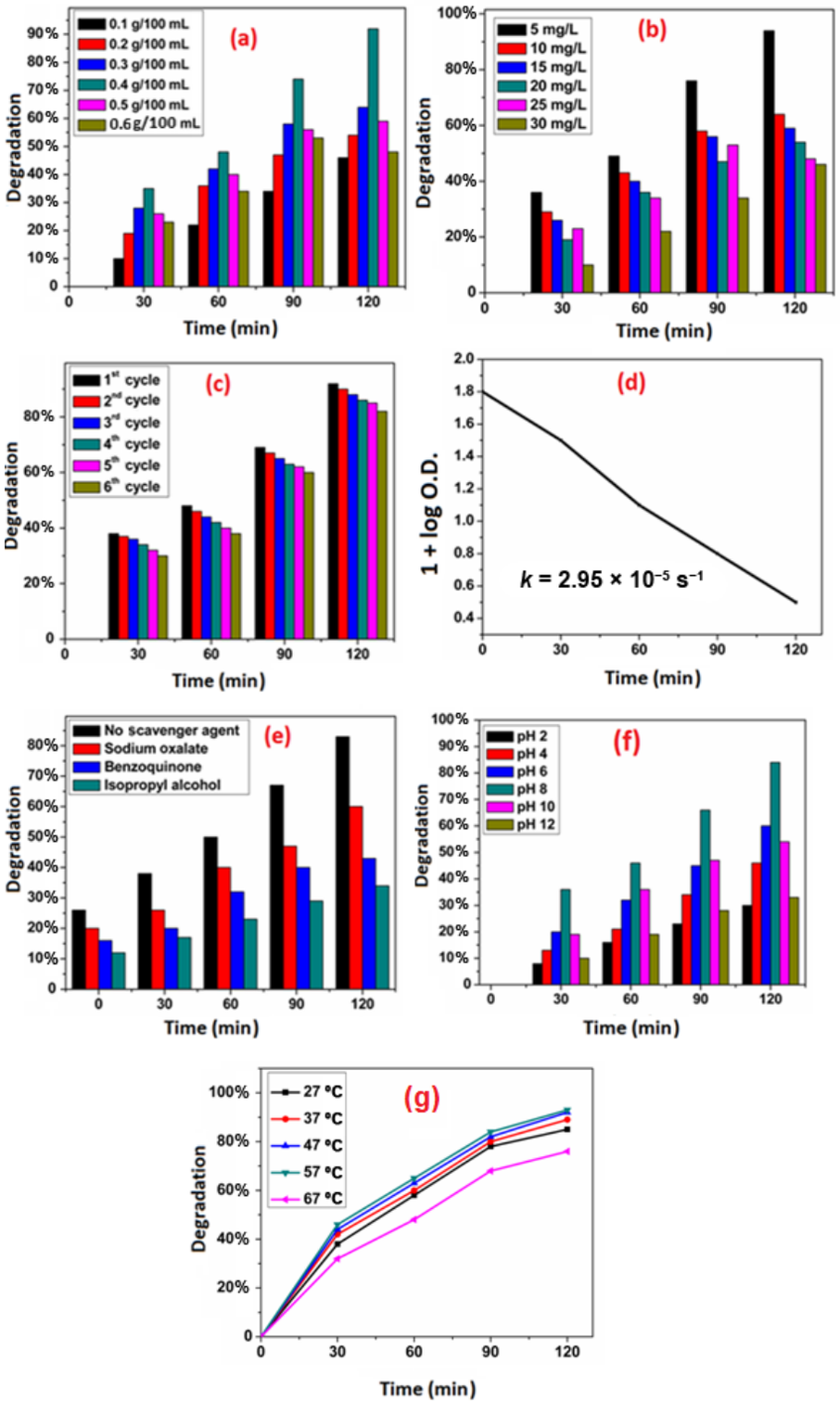

Fig. 19 Effects of **(a)** R_3TL catalytic load, **(b)** Evans blue dye concentration, **(c)** recyclability, **(d)** kinetic study, **(e)** scavenger study, **(f)** pH, and **(g)** temperature on the photocatalytic degradation of Evans blue dye by R_3TL.

caused by the high turbidity of slurry. The effect of Evans blue dye concentration on the photocatalytic activity of R_3TL was analyzed based on these experimental conditions: photocatalyst amount of 0.4 g/100 mL and pH 8 (Fig. 19(b)). As the dye concentration was increased, the time required for decaying the dye also increased due to increased adsorption of dye molecules on the R_3TL photocatalyst surface. The adsorbed dye molecules did not decay completely because lower number of hydroxyl and superoxide radicals was generated due to limited penetration of light.

The reusability of R_3TL as a photocatalyst was studied by extracting it after the first photocatalytic degradation of dye (Fig. 19(c)). R_3TL was washed twice and dried at 85 °C for 2 h. The dried powder was again used as a photocatalyst for the photocatalytic degradation of Evans blue dye. R_3TL was regenerated after almost 6 cycles of reuse. For the recyclability test, 0.4 g/100 mL and 5 mg/L of R_3TL and dye were used, respectively; the pH of the slurry was 8. Results revealed that the photocatalytic degradation of dyes by R_3TL decreased negligibly, probably because the Evans blue dye was accumulated on its surface. As a result, fewer surfaces were available for smooth photocatalytic decaying of dye, which eventually decreased the photocatalytic degradation rate. From the above recyclable studies, it was proved that the prepared R_3TL showed good photo and chemical stabilities. The kinetics of the photocatalytic degradation of Evans blue dye by R_3TL (Fig. 19(d)) was analyzed from the plot of 1 + log O.D. vs. irradiation time. An almost straight-line plot indicated that the photocatalytic degradation of Evans blue dye by R_3TL followed the pseudo first-order kinetic reaction with a rate constant (k) of 2.95×10^{-5} s^{-1}. Herein, radical (h^+ and super oxide radical and hydroxyl radical capture experiments were also conducted. Sodium oxalate, benzoquinone, and isopropyl alcohol were used as h^+, superoxide radical, and hydroxyl radical, scavenger, respectively [11]. As shown in Fig. 19(e), the photocatalytic degradation efficiency of Evans blue dye by R_3TL NCs considerably decreased after adding sodium oxalate into the photocatalytic reaction mixture; h^+ was the main active species in the reaction. The photocatalytic degradation rate of Evans blue decreased upon adding benzoquinone and isopropyl alcohol. The reduced photocatalytic degradation upon adding benzoquinone indicated that $\cdot O^{2-}$ has a certain effect on the Evans blue degradation. When isopropyl alcohol was added as the $\cdot OH$ scavenger, the degradation efficiency of Evans blue considerably decreased, indicating the substantial effect of $\cdot OH$ on the photocatalytic degradation of Evans blue dye. To determine the effect of pH on the photocatalytic degradation of Evans blue dye by R_3TL, the pH of the solution was regulated by adding 0.05-M H_2SO_4 and 0.1-N NaOH. Variations in the pH from 2 to 12 altered the surface properties of R_3TL (Fig. 19(f)). At pH 8, the highest photocatalytic degradation was achieved due to the formation of abundant hydroxyl radicals and hydrogen peroxide [13]. Figure 19(g) shows the effect of temperature on the photocatalytic degradation rate of the dye. Herein, the photocatalytic degradation was assessed at 5 reaction temperatures of 27, 37, 47, 57, and 67 °C. Results revealed that the photocatalytic degradation rate improved at higher temperatures. At 67 °C, the photocatalytic degradation rate considerably decreased due to increased charge carrier recombination, which further reduced the photocatalytic degradation rate. Thus, the temperature range of 25–57 °C is considered ideal for the effective photocatalytic degradation of organic dyes.

Antimicrobial activity of R_3TL and R_3TH

The antibacterial activities of R_3TL and R_3TH were screened against pathogenic bacterial strains. Pathogenic microbes have exhibited their pathogenicity in various disease and infections caused in humans such as *Bacillus* sp. (bacteremia and septicemia, wounds, abscesses, burns, and ear infections), *E. coli* (stomach cramps and diarrhea), *Pseudomonas aeruginosa* (nosocomial infection), *K. pneumonia* (meningitis and liver abscess), *S. aureus* (skin, soft tissue, and device-related infections), and *A. baumannii* (urinary tract, blood, lungs, and wounds). The zone of inhibition test was performed using Mueller–Hinton agar plates (Hi Media). Based on the derived inhibition patterns, the synthesized nanomaterials showed an excellent zone of inhibition (***$p < 0.001$) in several bacterial strains. Figures 20 and 21 show a clear zone of inhibition at considerably higher doses of R_3TL and R_3TH, i.e., 200 and 100 mg/mL, respectively. However, Gram-positive *S. aureus* exhibited remarkable increased zone of inhibition (35 mm) compared with all other strains used for R_3TH. Contrarily, *Bacillus* sp. exhibited the

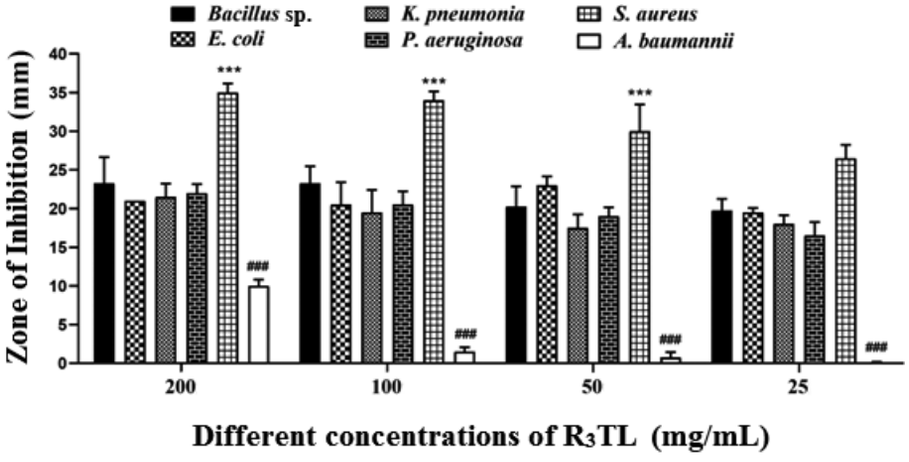

Fig. 20 Inhibition zone diameters (mm) of R_3TL against six pathogenic strains using the gel diffusion method. Values represent the mean S.E. for $n = 4$ replicates. ***$p < 0.001$ compared with all the other pathogenic strains used herein. ###$p < 0.001$ compared with all the other pathogenic strains used herein.

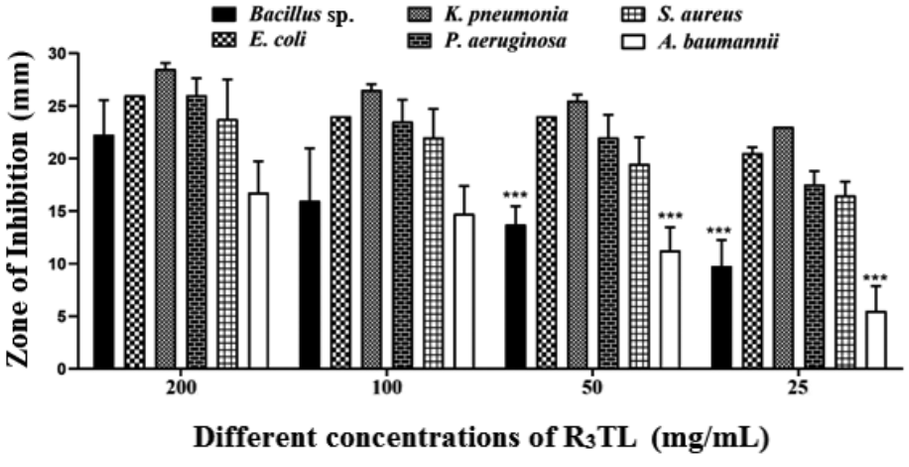

Fig. 21 Inhibition zone diameters (mm) of R_3TH against six pathogenic strains using the gel diffusion method. Values represent the mean S.E. for $n = 4$ replicates. ***$p < 0.001$ compared with all the other pathogenic strains used herein.

second largest zone of inhibition (21 mm) after *S. aureus* (34 mm) for R_3TL. R_3TH exhibited a similar antimicrobial effect on *E. coli, P. aeruginosa, K. pneumoniae*, and *S. aureus*; however, this effect was slightly inhibited in *Bacillus* sp. compared with R_3TL. This indicated a broad-spectrum action of the NPs used on the pathogenic strain of bacteria. R_3TL and R_3TH demonstrated cell lysis and microbial degradation by forming protein–NP complexes, thereby exhibiting broad-spectrum bactericidal activity. This is because NPs can release reactive oxygen species, which causes bacterial death by disrupting the cell wall, membrane, and organelle organization structures that lead to the loss of their physiological activities [27, 28]. Four organisms namely, *E. coli*, *P. aeruginosa*, *K. pneumoniae*, and *S. aureus* showed a good zone of inhibitions as the R_3TL and R_3TH concentrations were increased. *S. aureus* showed the largest zone of inhibition, whereas *A. baumannii* exhibited slightly larger zone of inhibition in the presence of R_3TL compared with R_3TH. This is because of the improved surface area, surface reactivity, and surface morphology of R_3TL compared with R_3TH. Figures 22 and 23 show the results of the antibacterial test of R_3TL and R_3TH against six pathogenic bacterial strains, respectively.

Conclusions

Herein, bare TiO_2 NPs and novel Ru/TiO_2 NCs were synthesized with and without ILs using the hydrothermal method at an incubation period of 24 h and at 130 °C. Then, their various parameters were compared during the synthesis of these nanomaterialsusing 1-butyl-2,3-dimethylimidazolium tetrafluoroborateas the IL and titanium (IV)

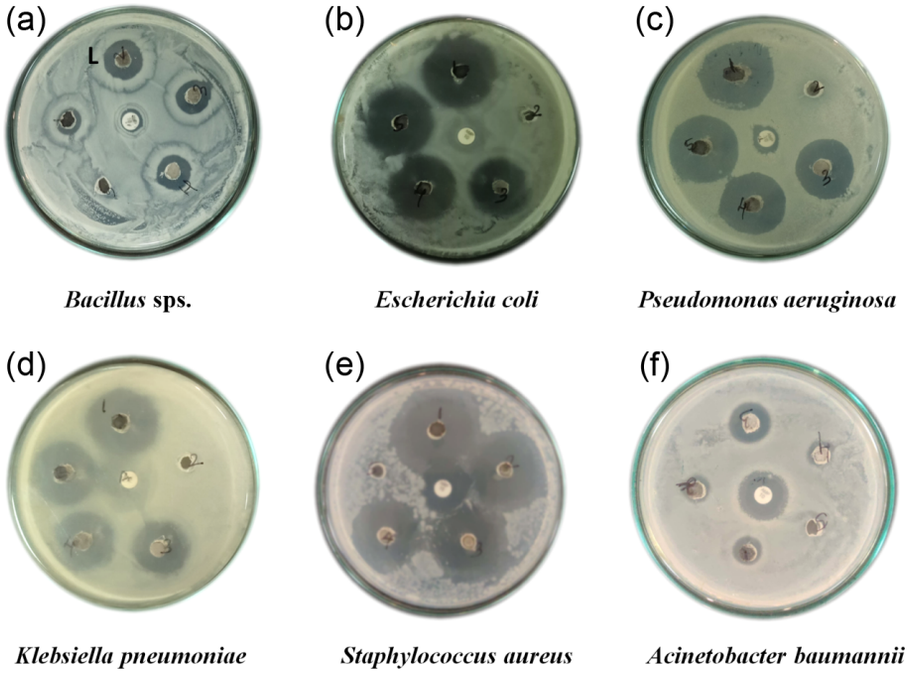

Fig. 22 Antibacterial activity of R_3TL with **(a)** *Bacillus* sps., **(b)** *E. coli*, **(c)** *P. aeruginosa*, **(d)** *K. pneumonia*, **(e)** *S. aureus*, and **(f)** *A. baumannii.* Dilution used 1–200 mg/mL, 2–100 mg/mL, 3–50 mg/mL, 4–25 mg/mL, 5-negative control (autoclaved distilled water), and center Ampicillin as positive control.

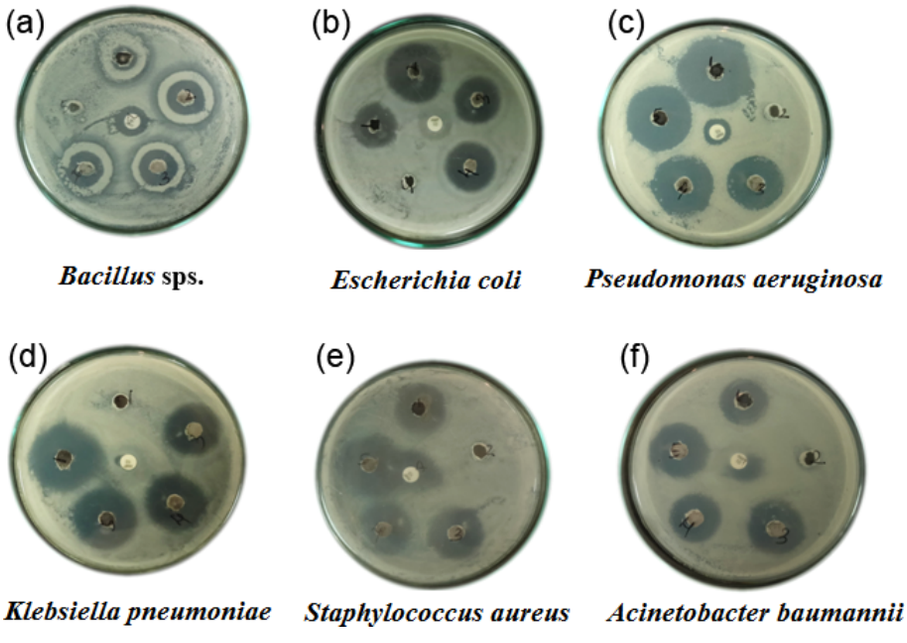

Fig. 23 Antibacterial activity of R_3TH with **(a)** *Bacillus* sps., **(b)** *E. coli*, **(c)** *P. aeruginosa*, **(d)** *K. pneumonia*, **(e)** *S. aureus*, and **(f)** *A. baumannii.* Dilution used 1–200 mg/mL, 2–100 mg/mL, 3–50 mg/mL, 4–25 mg/mL, 5-negative control (autoclaved distilled water), and center ampicillin as positive control.

isopropoxide and ruthenium(III) nitrate as the precursors. The prepared NCs were compared using various characterization methods for assessing their photocatalytic degradation and antibacterial activity. PXRD and TEM analyses confirmed the anatase and rutile phases as well as the nanocrystalline structure of Ru/TiO_2 NCs. The chemical composition verified via XPS and EDS revealed the existence of Ru, Ti, and O in the synthesized Ru/TiO_2 NCs. The optical properties and bandgap energies of Ru/TiO_2 NCs were determined via UV–Vis diffuse reflectance spectroscopy, which revealed that the optical properties exhibited a red shift in their optical response toward the visible region due to the reduced

bandgap energy of Ru/TiO_2 NCs in the visible region. The amount of Ru in the TiO_2 structure was modified for enhancing the photocatalytic and antibacterial activities of the NCs. Among the various doping concentrations of Ru in the TiO_2 structure, 0.3 wt% was considered ideal because the composite showed the highest BET surface area compared with other samples. PL spectra showed a decrease in the PL intensity of R_3TL, which effectively controlled the recombination of photoexcited electrons and holes compared with other NCs. As a result, R_3TL was considered an ideal photocatalyst and used for subsequent studies. The optimized Ru/TiO_2 NCs exhibited high photocatalytic degradation ability toward the Evans blue dye, with a maximum dye removal rate of 97.22% within 120 min under visible light irradiation. The effect of pH, catalytic load, dye concentration, illumination intensity, scavenger types on the recyclability and reusability of dye by Ru/TiO_2 NCs was analyzed. Scavenging experiments indicated that $\cdot O^{2-}$ and ·OH were important radical species and mainly responsible for photocatalytic degradation. Ru/TiO_2 NCs showed an appreciable antibacterial activity against a few Gram-positive strains and Gram-negative strains of bacteria. In summary, Ru/TiO_2 NCs synthesized using the IL-assisted hydrothermal method exhibited enhanced photocatalytic and antibacterial activities compared with the hydrothermal method, highlighting the importance of ILs.

CRediT Author Statement

T.N. Ravishankar: methodology, supervision, writing original draft, writing–review & editing, data creation, investigation, and formal analysis. **A. Ananda**: formal analysis, methodology, writing original draft. **J.R. Adarsha**: conceptualization, investigation, methodology, project administration. **B.M. Shilpa**: conceptualization, funding acquisition, investigation, project administration, resources, supervision, and validation.

Acknowledgements

Dr. T.N. Ravishankar, wish to acknowledge the Laboratory of Thin Films and Nanostructure Fabrication (L3F nano), Institute of Physics, UFRGS, Brazil for the research facilities.

Conflict of Interests

The authors declare that no competing interest exists.

References

[1] A.T. Yassen, K.K. Khudair, M.A.M. Hassan. Piperine loaded titanium dioxide nanoparticles: Development, characterisation and biomedical application. *Nano Biomedicine and Engineering*, 2022, 14(2): 192−200. https://doi.org/10.5101/nbe.v14i2.p192-200

[2] T.N. Ravishankar, M. de O Vaz, T. Ramakrishnappa, et al. Ionic liquid–assisted hydrothermal synthesis of Nb/TiO_2 nanocomposites for efficient photocatalytic hydrogen production and photodecolorization of Rhodamine B under UV-visible and visible light illuminations. *Materials Today Chemistry*, 2019, 12: 373−385. https://doi.org/10.1016/j.mtchem.2019.04.001

[3] A. Hassani, L. Alidokht, A.R. Khataee, et al. Optimization of comparative removal of two structurally different basic dyes using coal as a low-cost and available adsorbent. *Journal of the Taiwan Institute of Chemical Engineers*, 2014, 45(4): 1597−1607. https://doi.org/10.1016/j.jtice.2013.10.014

[4] E. Ayranci, O. Duman. *In-situ* UV-visible spectroscopic study on the adsorption of some dyes onto activated carbon cloth. *Separation Science and Technology*, 2009, 44(15): 3735−3752. https://doi.org/10.1080/01496390903182891

[5] D.T. Nguyen, S.S. Hong. The effect of solvent on the synthesis of BiVO4 using solvothermal method and their photocatalytic activity under visible light irradiation. *Topics in Catalysis*, 2017, 60(9): 782−788. https://doi.org/10.1007/s11244-017-0770-8

[6] X.D. Zhang, Y.X. Wang, F.L. Hou, et al. Effects of Ag loading on structural and photocatalytic properties of flower-like ZnO microspheres. *Applied Surface Science*, 2017, 391: 476−483. https://doi.org/10.1016/j.apsusc.2016.06.109

[7] R. Ashouri, P. Ghasemipoor, B. Rasekh, et al. The effect of ZnO-based carbonaceous materials for degradation of benzoic pollutants: A review. *International Journal of Environmental Science and Technology*, 2019, 16(3): 1729−1740. https://doi.org/10.1007/s13762-018-2056-5

[8] J.R. Adarsha, T.N. Ravishankar, A. Ananda, et al. Hydrothermal synthesis of novel heterostructured $Ag/TiO_2/CuFe_2O_4$ nanocomposite: Characterization, enhanced photocatalytic degradation of methylene blue dye, and efficient antibacterial studies. *Water Environment Research*, 2022, 94(6): e10744. https://doi.org/10.1002/wer.10744

[9] S. Chen, D.L. Huang, P. Xu, et al. Facet-engineered surface and interface design of monoclinic scheelite bismuth vanadate for enhanced photocatalytic performance. *ACS Catalysis*, 2020, 10(2): 1024−1059. https://doi.org/10.1021/acscatal.9b03411

[10] H.A. Ewais. Kinetics and mechanism of the formation of silver nanoparticles by reduction of silver (I) with maltose in the presence of some active surfactants in aqueous medium. *Transition Metal Chemistry*, 2014, 39(5): 487−493. https://doi.org/10.1007/s11243-014-9823-z

[11] S. Chairam, W. Konkamdee, R. Parakhun. Starch-supported gold nanoparticles and their use in 4-nitrophenol reduction. *Journal of Saudi Chemical Society*, 2017, 21(6): 656−663. https://doi.org/10.1016/j.jscs.2015.11.001

[12] S. Alkaykh, A. Mbarek, E.E. Ali-Shattle. Photocatalytic degradation of methylene blue dye in aqueous solution by

$MnTiO_3$ nanoparticles under sunlight irradiation. *Heliyon*, 2020, 6(4): e03663. https://doi.org/10.1016/j.heliyon.2020.e03663

[13] A. Molla, M. Sahu, S. Hussain. Under dark and visible light: Fast degradation of methylene blue in the presence of Ag–In–Ni–S nanocomposites. *Journal of Materials Chemistry A*, 2015, 3(30): 15616−15625. https://doi.org/10.1039/c5ta02888d

[14] E. Brillas, C.A. Martínez-Huitle, Decontamination of wastewaters containing synthetic organic dyes by electrochemical methods. An updated review. *Applied Catalysis B: Environmental*, 2015, 166–167: 603–643. https://doi.org/10.1016/j.apcatb.2014.11.016

[15] C.X. Gui, Q.Q. Wang, S.M. Hao, et al. Sandwichlike magnesium silicate/reduced graphene oxide nanocomposite for enhanced Pb^{2+} and methylene blue adsorption. *ACS Applied Materials & Interfaces*, 2014, 6(16): 14653−14659. https://doi.org/10.1021/am503997e

[16] V.V. Atuchin, V.A. Golyashov, K.A. Kokh, et al. Formation of inert Bi_2Se_3(0001) cleaved surface. *Crystal Growth & Design*, 2011, 11(12): 5507−5514. https://doi.org/10.1021/cg201163v

[17] S. Tunç, T. Gürkan, O. Duman. On-line spectrophotometric method for the determination of optimum operation parameters on the decolorization of Acid Red 66 and Direct Blue 71 from aqueous solution by Fenton process. *Chemical Engineering Journal*, 2012, 181–182: 431–442. https://doi.org/10.1016/j.cej.2011.11.109

[18] S. Kai, X. Xin,W. Xiaoyi, et al. One-step synthesis of band-tunable N, S Co-doped commercial TiO_2/graphene quantum dots composites with enhanced photocatalytic activity. *RSC Advances*, 2017, 7(38): 23319−23327. https://doi.org/10.1039/c7ra01856h

[19] F.S. Aljohani, M. Elsafi, N.I. Ghoneim, et al. Water treatment from MB using Zn-Ag MWCNT synthesized by double arc discharge. *Materials*, 2021, 14(23): 7205. https://doi.org/10.3390/ma14237205

[20] S.S. Ali, R. Al-Tohamy, R.R. Xie, et al. Construction of a new lipase- and xylanase-producing oleaginous yeast consortium capable of reactive azo dye degradation and detoxification. *Bioresource Technology*, 2020, 313: 123631. https://doi.org/10.1016/j.biortech.2020.123631

[21] W.B. Wang, G.Y. Tian, Z.F. Zhang, et al. A simple hydrothermal approach to modify palygorskite for high-efficient adsorption of Methylene blue and Cu(II) ions. *Chemical Engineering Journal*, 2015, 265: 228−238. https://doi.org/10.1016/j.cej.2014.11.135

[22] M. Ismael. Highly effective ruthenium-doped TiO_2 nanoparticles photocatalyst for visible-light-driven photocatalytic hydrogen production. *New Journal of Chemistry*, 2019, 43(24): 9596−9605. https://doi.org/10.1039/c9nj02226k

[23] Z.W. Sun, C. Srinivasakannan, J.S. Liang, et al. Preparation of hierarchical magnesium silicate with excellent adsorption capacity. *Ceramics International*, 2019, 45(4): 4590−4595. https://doi.org/10.1016/j.ceramint.2018.11.146

[24] Y.X. Jin, Z. Liu, L. Han, et al. Synthesis of coal-analcime composite from coal gangue and its adsorption performance on heavy metal ions. *Journal of Hazardous Materials*, 2022, 423: 127027. https://doi.org/10.1016/j.jhazmat.2021.127027

[25] D.W. Lan, H.W. Zhu, J.W. Zhang, et al. Adsorptive removal of organic dyes via porous materials for wastewater treatment in recent decades: A review on species, mechanisms and perspectives. *Chemosphere*, 2022, 293: 133464. https://doi.org/10.1016/j.chemosphere.2021.133464

[26] C. Cassol, G. Ebeling, B. Ferrera, et al. A simple and practical method for the preparation and purity determination of halide-free imidazolium ionic liquids. *Advanced Synthesis & Catalysis*, 2006, 348(1-2): 243−248. https://doi.org/10.1002/adsc.200505295

[27] S. Borehalli Mayegowda, A. Roy, N.G. Manjula, et al. Eco-friendly synthesized nanoparticles as antimicrobial agents: An updated review. *Frontiers in Cellular and Infection Microbiology*, 2023, 13: 1224778. https://doi.org/10.3389/fcimb.2023.1224778

[28] S.B. Mayegowda, G. Sarma, M.N. Gadilingappa, et al. Green-synthesized nanoparticles and their therapeutic applications: A review. *Green Processing and Synthesis*, 2023, 12(1): 20230001. https://doi.org/10.1515/gps-2023-0001